slabs without any adsorbate (F_0), with only CO_2 (F_{CO_2}), with only AQ (F_{aq}), and with AQ and CO_2 (F_{both}): $F_{inter} = F_{both} + F_0 - F_{CO_2} - F_{aq} \approx$ 0.12 eV. This interaction is mediated by the substrate (26–30) rather than involving a direct intermolecular bond; its energy correlates well with the occasional observation of spontaneous separation at ≥ 50 K.

The velocity of AQ decreases when it carries a CO_2 load. From temperature-dependent measurements of hundreds of steps of AQ (with zero, one, or two CO_2 molecules attached), we obtained the Arrhenius plot shown in Fig. 4. It indicates that the diffusion barrier for AQ of ~0.02 eV increases by ~0.03 eV upon attachment of the first CO_2 molecule and by an additional ~0.02 eV for the second molecule, thus roughly doubling and tripling, respectively. Although the diffusion barriers of Fig. 4 are very low in absolute terms, they correspond well with other species and complexes on Cu(111) [e.g., Cu atoms, 0.037 eV (30); CO chevrons, 0.010 eV] (31).

AQ's ability to reversibly attach CO_2 provides a means for transport of CO_2 molecules along a line from point A to point B on a surface, as long as A and B are connected by any of the three Cu(111) high-symmetry directions. This result is in stark contrast to CO_2's native isotropic

diffusion. As such, our observations are proof of principle for the application of molecules at surfaces as molecular-scale analogs of macroscopic machinery ("molecular machines")—that is, as entities that change the position or properties of separate, molecular-scale objects in a predetermined fashion.

References and Notes

1. J. S. Moore, *Acc. Chem. Res.* **30**, 402 (1997).
2. G. S. Kottas, L. I. Clarke, D. Horinek, J. Michl, *Chem. Rev.* **105**, 1281 (2005).
3. J. P. Collin, C. Dietrich-Buchecker, P. Gavina, M. C. Jimenez-Molero, J. P. Sauvage, *Acc. Chem. Res.* **34**, 477 (2001).
4. J. K. Gimzewski *et al.*, *Science* **281**, 531 (1998).
5. Y. Shirai, A. J. Osgood, Y. M. Zhao, K. F. Kelly, J. M. Tour, *Nano Lett.* **5**, 2330 (2005).
6. K. Y. Kwon *et al.*, *Phys. Rev. Lett.* **95**, 166101 (2005).
7. R. Otero *et al.*, *Angew. Chem. Int. Ed.* **43**, 2092 (2004).
8. L. Gross *et al.*, *Phys. Rev. Lett.* **93**, 056103 (2004).
9. V. Balzani, A. Credi, F. M. Raymo, J. F. Stoddart, *Angew. Chem. Int. Ed.* **39**, 3348 (2000).
10. R. A. van Delden *et al.*, *Nature* **437**, 1337 (2005).
11. T. R. Kelly, H. De Silva, R. A. Silva, *Nature* **401**, 150 (1999).
12. J. V. Barth, G. Costantini, K. Kern, *Nature* **437**, 671 (2005).
13. F. Rosei *et al.*, *Prog. Surf. Sci.* **71**, 95 (2003).
14. S. J. Stranick, M. M. Kamna, P. S. Weiss, *Science* **266**, 99 (1994).
15. R. Otero *et al.*, *Nat. Mater.* **3**, 779 (2004).
16. J. A. Theobald, N. S. Oxtoby, M. A. Phillips, N. R. Champness, P. H. Beton, *Nature* **424**, 1029 (2003).
17. H. Brune, M. Giovannini, K. Bromann, K. Kern, *Nature* **394**, 451 (1998).
18. S. Horch *et al.*, *Nature* **398**, 134 (1999).
19. G. S. McCarty, P. S. Weiss, *J. Am. Chem. Soc.* **126**, 16772 (2004).
20. A corresponding movie appears on *Science* Online.
21. K. H. Ernst, D. Schlatterbeck, K. Christmann, *Phys. Chem. Chem. Phys.* **1**, 4105 (1999).
22. G. Kresse, J. Hafner, *Phys. Rev. B* **47**, 558 (1993).
23. J. Perdew, Y. Wang, *Phys. Rev. B* **45**, 13244 (1992).
24. M. Payne, M. Teter, D. Allan, T. Arias, J. Joannopoulos, *Rev. Mod. Phys.* **64**, 1045 (1992).
25. D. Vanderbilt, *Phys. Rev. B* **41**, 7892 (1990).
26. E. C. H. Sykes *et al.*, *Acc. Chem. Res.* **36**, 945 (2003).
27. T. Mitsui, M. K. Rose, E. Fomin, D. F. Ogletree, M. Salmeron, *Phys. Rev. Lett.* **94**, 036101 (2005).
28. S. Lukas, G. Witte, C. Woll, *Phys. Rev. Lett.* **88**, 028301 (2002).
29. G. Pawin, K. L. Wong, K. Y. Kwon, L. Bartels, *Science* **313**, 961 (2006).
30. J. Repp *et al.*, *Phys. Rev. Lett.* **85**, 2981 (2000).
31. A. J. Heinrich, C. P. Lutz, J. A. Gupta, D. M. Eigler, *Science* **298**, 1381 (2002).
32. Supported by U.S. Department of Energy joint grants DE-FGO2-03ER15464/5. We thank the Academic Associates Program of the San Diego Supercomputer Center for computational resources.

Multifunctional Encoded Particles for High-Throughput Biomolecule Analysis

Daniel C. Pregibon,[1] Mehmet Toner,[2] Patrick S. Doyle[1]*

High-throughput screening for genetic analysis, combinatorial chemistry, and clinical diagnostics benefits from multiplexing, which allows for the simultaneous assay of several analytes but necessitates an encoding scheme for molecular identification. Current approaches for multiplexed analysis involve complicated or expensive processes for encoding, functionalizing, or decoding active substrates (particles or surfaces) and often yield a very limited number of analyte-specific codes. We present a method based on continuous-flow lithography that combines particle synthesis and encoding and probe incorporation into a single process to generate multifunctional particles bearing over a million unique codes. By using such particles, we demonstrate a multiplexed, single-fluorescence detection of DNA oligomers with encoded particle libraries that can be scanned rapidly in a flow-through microfluidic channel. Furthermore, we demonstrate with high specificity the same multiplexed detection using individual multiprobe particles.

The ability to quantify multiple proteins, cytokines, or nucleic acid sequences in parallel using a single sample allows researchers and clinicians to obtain high-density information with minimal assay time, sample volume, and cost. Such multiplexed analysis is accompanied by several challenges, including molecular encoding and the need to retain assay sensitivity, specificity, and reproducibility with the use of complex mixtures. There are two broad classes of technologies used for multiplexing: planar arrays (1–3) and suspension (particle-based) arrays (4–21), both of which have application-specific advantages. Planar arrays, such as DNA and protein microarrays, are best suited for

applications requiring ultra-high-density analysis. In comparison, suspension arrays benefit from solution kinetics, ease of assay modification, higher sample throughput, and better quality control by batch synthesis (22). Although particle-based arrays have been used for high-density genotyping applications (23), they are most favorable over microarrays when detecting a modest number of targets over large populations or when rapid probe-set modification is desired. Whereas planar arrays rely strictly on positional encoding, suspension arrays have used a great number of encoding schemes that can be classified as spectrometric (4–11), graphical (12–16), electronic (17–19), or physical (20, 21).

Spectrometric encoding uses specific wavelengths of light or radiation [including fluorophores (4–7), chromophores (8), photonic structures (9), and Raman tags (10, 11)] to identify a species. Fluorescence-encoded microbeads (4–7) can be rapidly processed by using conventional flow cytometry [or on fiber-optic arrays (24)], making them a popular platform for multiplexing. However, there are several disadvantages of using multiple fluorescent signals as means of barcoding, including (i) the limited barcodes achievable (typically ~100) because of spectral overlap, (ii) the lack of portability for bulky flow cytometers, (iii) added cost with each fluorescent exciter and detector needed, and (iv) potential interference of encoding fluorescence with analyte-detection fluorescence. For these reasons, single-fluorescence methods

[1]Department of Chemical Engineering, Massachusetts Institute of Technology, Cambridge, MA 02139, USA. [2]BioMEMS Resource Center and Center for Engineering in Medicine, Massachusetts General Hospital, and Harvard Medical School, Boston, MA 02114, USA.

*To whom correspondence should be addressed. E-mail: pdoyle@mit.edu

exist that use graphical techniques to spatially embed barcodes on microcarriers.

Graphical barcodes rely on the patterning of optical elements on a microcarrier; some examples include striped rods (12, 13), ridged particles (14), and dot-patterned particles (14, 15). The chemistries used to fabricate such particles (metallic or photoresist) require additional coupling chemistries to conjugate biomolecules to the surface, and, in the case of striped rods, each metallic pattern needs to be generated one batch at a time. Typically, the patterns on these particles can only be distinguished if the fluorescence of the target signal is sufficiently high. Another graphical method for microcarrier encoding is the selective photobleaching of codes into fluorescent beads (16). In this method, both particle synthesis and decoding are time-consuming, making it an unlikely candidate for high-throughput analysis. A method that eliminates fluorescence altogether uses radio frequency memory tags (17–19). This approach is very powerful because it allows for nearly unlimited barcodes (>10^{12}) and decouples the barcoding scheme from analyte quantification (fluorescence), but the synthesis of any appreciable number (thousands or millions) of these electronic microchip-based carriers may prove to be expensive and slow. These and several other methods developed for multiplexed analysis have been thoroughly reviewed elsewhere (25, 26).

We introduce a technique that overcomes many of these multiplexing limitations. By exploiting laminar flows characteristic of microfluidics, we demonstrate the ability to generate multifunctional particles with distinct regions for analyte encoding and target capture (Fig. 1). In a typical experiment, we flowed two monomer streams (one loaded with a fluorescent dye and the other with an acrylate-modified probe) adjacently down a microfluidic channel and used a variation of continuous-flow lithography (27) to polymerize particles [with 30-ms bursts of ultraviolet (UV) light] across the streams (28) (movie S1). In this manner, particles with a fluorescent, graphically encoded region and a probe-loaded region can be synthesized in a single step. Each particle is an extruded two-dimensional (2D) shape (Fig. 1B) whose morphology is determined by a photomask that is inserted into the field-stop position of the microscope and whose chemistry is determined by the content of the coflowing monomer streams. The cross-linked polymer particles then flow down the channel [without sticking due to oxygen inhibition near the channel surfaces (27)], where they are collected in a reservoir. The particles can be rinsed of excess monomer and then used for biological assays.
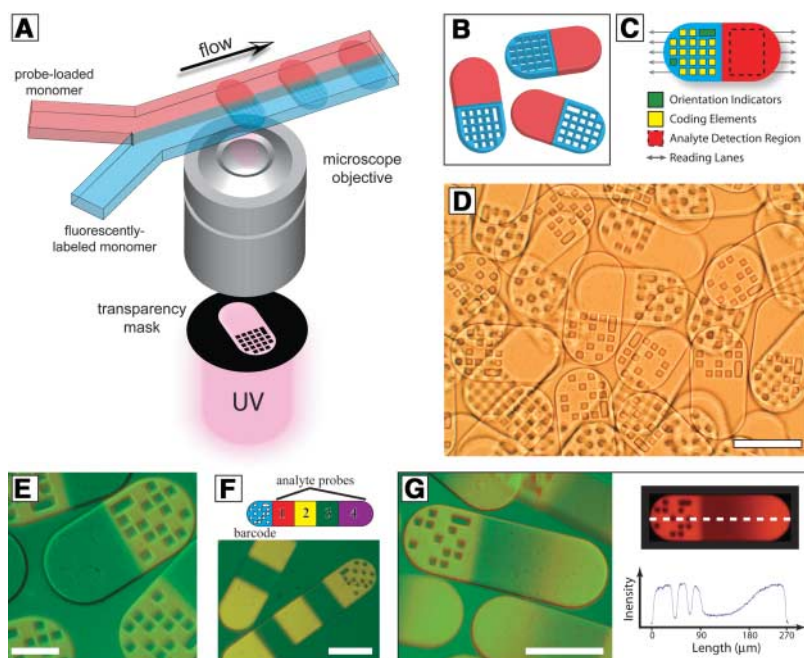
We used poly(ethylene glycol) (PEG) (well known as a bio-inert polymer) as the particle foundation to eliminate the need to "block" surfaces after probe conjugation and as a transparent material to allow transmission of fluorescent signal from both particle faces. These properties

should enhance both specificity and sensitivity of analyte detection. We used a simple dot-coding scheme to generate particles that can bear over a million (2^{20}) codes (Fig. 1C). Particles were designed to be "read" along five lanes down their length, with alignment indicators that were used to identify the code position and the read "direction" despite the particle orientation (Fig. 1C). The flat, long shape of the particles helps align them for scanning in a flow-through device. The spatial separation of various chemistries on the particles allows decoding and target detection to be achieved by using a single fluorophore.

To demonstrate the versatility of particle synthesis, we selectively labeled monomer streams with a fluorophore and used a variety of channel designs to generate particles bearing a single probe region, multiple probe regions, and probe-region gradients (Fig. 1, E to G). Multiprobe particles (Fig. 1F), made with the use of channels with several inlet streams, allow for a direct, single-particle comparison of several targets. Furthermore, probe gradients (Fig. 1G), made by simply allowing diffusion of the probe across streams in a long channel, are useful for broadening the detection range of an analyte when using a fixed detection sensitivity (when the signal can saturate). If magnetic nanoparticles are incorporated in a gradient, it may be possible to produce a temperature variation along particles when stimulated in an oscillating magnetic field (29).

A key feature of our method is the direct incorporation of probes into the encoded particles. This is accomplished by simply adding acrylate-modified biomolecules into the monomer solution. After polymerization, the probes are covalently coupled to the polymer network. This process is applicable for both oligonucleotide and protein probes (30–32). We demonstrate that the short bursts of UV used to synthesize probe-conjugated particles are not detrimental to the functionality of incorporated oligonucleotides. Previously, we showed similar results with bead-bound antibodies that were incorporated into polymer structures made from nearly identical monomer constituents (28, 33).

To demonstrate multiplexing capabilities, we used acrylate-modified oligonucleotide probes (which are commercially available) for DNA sequence detection (Fig. 2, A to C). We synthesized three batches of particles: one of which was loaded with 20–base pair (bp) oligonucleotide probe 1 (5′-ATA GCA GAT CAG CAG CCA GA-3′), another with probe 2 (5′-CAC TAT GCG CAG GTT CTC AT-3′), and a third with no probe, to serve as a control. Targets were fluorescently labeled oligonucleotides with complementary sequences to the two probes. We mixed the particles and incubated them for 10 min at room temperature in microwells containing either target 1 (at 1 μM), target 2 (at 1 μM), both targets (both at 0.5 μM), or no target (28). A positive target

Fig. 1. (**A**) Schematic diagram of dot-coded particle synthesis showing polymerization across two adjacent laminar streams to make single-probe, half-fluorescent particles [shown in (**B**)]. (**C**) Diagrammatic representation of particle features for encoding and analyte detection. Encoding scheme shown allows the generation of 2^{20} (1,048,576) unique codes. (**D**) Differential interference contrast (DIC) image of particles generated by using the scheme shown in (A). (**E** to **G**) Overlap of fluorescence and DIC images of single-probe (**E**), multiprobe (**F**, bottom), and probe-gradient (**G**, left) encoded particles. Shown also is a schematic representation of multiprobe particles (F, top) and a plot of fluorescent intensity along the center line of a gradient particle (G, right). Scale bars indicate 100 μm in (D), (F), and (G) and 50 μm in (E).

detection was indicated by probe-region fluorescence, which was more pronounced near the particle edges. This result suggested that targets were able to diffuse and hybridize several μm into the particle body (28). In each instance, the particles

showed uniformity (28) with high specificity to the oligomers, exhibiting fluorescence only when the target was present (Fig. 2C).

To further demonstrate the power of our multiplexing scheme, we performed the same sequence detection assay with the use of particles with multiple adjacent functionalities (Fig. 2, D to F). In this manner, we were able to simultaneously assay for the two target sequences (with a negative control) on a single particle. Again, the assay was highly specific (Fig. 2F) and very uniform from particle to particle (Fig. 2D) (28). The interfaces between probes on the particles are very sharp, and thinner stripes could be used for even greater multiplexing capabilities.
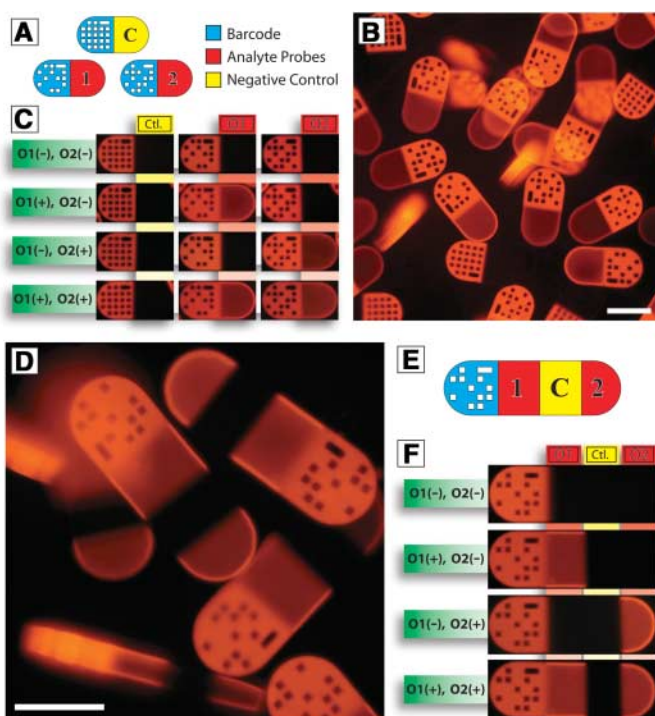
In order to prove that this method of multiplexed analysis is practical for high-throughput applications, we developed a simple scheme to scan particles in a flow-through device (Fig. 3). Multiprobe particles used in the hybridization experiment just described (Fig. 2, D to F) were flowed through a microfluidic channel and observed on an inverted fluorescence microscope (28). Particles were aligned by using flow-focusing and traveled down a channel only slightly larger than the particle width (Fig. 3A). We used a bio-friendly surfactant (28) to ensure that the particles flowed smoothly down the channels without sticking. Images were taken at a designated detection region in the channel with an exposure of 1/125 s as the particles passed the field of view (using a 20× objective). Image sequences were later analyzed to determine the particle code and quantify targets (movie S2).

A representative particle image is shown (Fig. 3B) with corresponding intensity plots along the five particle "reading lanes." The code along each lane can be determined by analyzing the sharp dips and plateaus in the intensity plots. By using the control-region fluorescence, we defined a positive target detection as the control average intensity plus three standard deviations for each particle. We were able to accurately identify the presence of both oligonucleotide targets after only a short 10-min incubation.
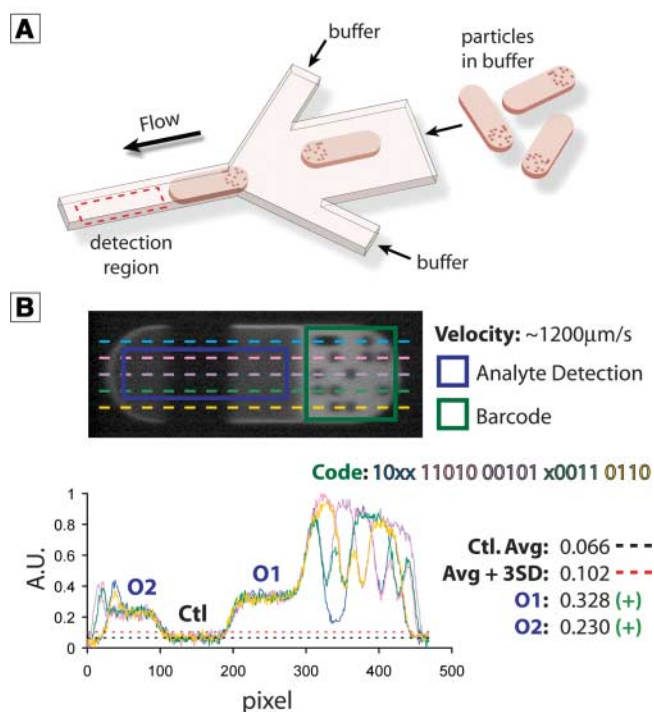
The throughput of our system is primarily determined by the detection scheme and the particle size. The particles synthesized for this study are relatively large compared with those in other flow-through methods, measuring 90 μm in width, ~30 μm in thickness, and 180 to 270 μm in length. Large size not only limits the throughput of a system but also increases the sample volume. However, the great particle-to-particle reproducibility we have demonstrated (28) will afford a much lower redundancy than is typical in flow-through systems, improving efficiency. By using conservative estimates, we found that our system should be capable of providing rapid, high-density analysis with a manageable sample volume (28) despite the seemingly large particle size.

In addition to being very reproducible, we have also shown that our system is very sensitive. With 30-min incubations, we can detect DNA oligomers comfortably at 500 attomoles without biotin-avidin–aided signal amplification (28). This leads us to believe that our system will be at least as sensitive as current, commercially available multiplexing technologies, with the added advan-

Fig. 2. Multiplexed analysis using single-(**A** to **C**) and multiprobe (**D** to **F**) encoded particles. The particles were loaded with DNA oligomer probes (O1, 5'-ATA GCA GAT CAG CAG CCA GA-3', or O2, 5'-CAC TAT GCG CAG GTT CTC AT-3') or no probe [negative control (C)] as shown schematically in (A) and (E). Shown are representative fluorescence images for single-probe (B) and multiprobe (D) particles after a 10-min incubation with both fluorescent-labeled targets. Fluorescence in the probe regions indicates target detection. Also shown are individual particles after incubation in solutions containing no targets, target 1 only, target 2 only, or both targets [(C) and (F)]. Scale bars, 100 μm.

Fig. 3. Flow-through particle reading. (**A**) Schematic representation of a flow-focusing microfluidic device used to align and read particles after hybridization experiments. Particles are directed down a narrow channel and are imaged by using fluorescence microscopy. (**B**) A typical image of a particle taken in a flow-through device as shown in (A). The image was captured by using a microscope-mounted camera with an exposure of 1/125 s as the particle flowed at a velocity of ~1200 μm/s through the channel. Scans of fluorescent intensity were taken across the five lanes of the particle to reveal the code and detect oligomer targets (O1 and O2). With the particle in this orientation, the code is read from right to left and top to bottom, where 1, 0, and x represent a hole, no hole, and an alignment marker, respectively. Particle shown is 90 μm by 270 μm. A.U., arbitrary units.

tages of all-in-one particle synthesis, incorporation of multiple probes, low cost (28), virtually unlimited codes, and implementation using little more than a standard fluorescence microscope.

References and Notes
1. D. Gershon, *Nature* **416**, 885 (2002).
2. S. P. Fodor *et al.*, *Nature* **364**, 555 (1993).
3. G. MacBeath, S. L. Schreiber, *Science* **289**, 1760 (2000).
4. R. J. Fulton, R. L. McDade, P. L. Smith, L. J. Kienker, J. R. Kettman Jr., *Clin. Chem.* **43**, 1749 (1997).
5. B. J. Battersby *et al.*, *J. Am. Chem. Soc.* **122**, 2138 (2000).
6. H. Xu *et al.*, *Nucleic Acids Res.* **31**, e43 (2003).
7. M. Han, X. Gao, J. Z. Su, S. Nie, *Nat. Biotechnol.* **19**, 631 (2001).
8. X. W. Zhao *et al.*, *Chem. Mater.* **18**, 2443 (2006).
9. F. Cunin *et al.*, *Nat. Mater.* **1**, 39 (2002).
10. X. Su *et al.*, *Nano Lett.* **5**, 49 (2005).
11. H. Fenniri, S. Chun, L. Ding, Y. Zyrianov, K. Hallenga, *J. Am. Chem. Soc.* **125**, 10546 (2003).
12. S. R. Nicewarner-Peña *et al.*, *Science* **294**, 137 (2001).
13. M. Y. Sha *et al.*, *Anal. Bioanal. Chem.* **384**, 658 (2006).
14. M. Evans, C. Sewter, E. Hill, *Assay Drug Dev. Technol.* **1**, 199 (2003).
15. Z. L. Zhi, Y. Morita, Q. Hasan, E. Tamiya, *Anal. Chem.* **75**, 4125 (2003).
16. K. Braeckmans *et al.*, *Nat. Mater.* **2**, 169 (2003).
17. E. J. Moran *et al.*, *J. Am. Chem. Soc.* **117**, 10787 (1995).
18. K. C. Nicolaou, X. Y. Xiao, Z. Parandoosh, A. Senyei, M. P. Nova, *Angew. Chem. Int. Ed.* **34**, 2289 (1995).
19. R. F. Service, *Science* **270**, 577 (1995).
20. T. M. McHugh, R. C. Miner, L. H. Logan, D. P. Stites, *J. Clin. Microbiol.* **26**, 1957 (1988).
21. A. R. Vaino, K. D. Janda, *Proc. Natl. Acad. Sci. U.S.A.* **97**, 7692 (2000).
22. J. P. Nolan, L. A. Sklar, *Trends Biotechnol.* **20**, 9 (2002).
23. J. B. Fan, M. S. Chee, K. L. Gunderson, *Nat. Rev. Genet.* **7**, 632 (2006).
24. J. A. Ferguson, F. J. Steemers, D. R. Walt, *Anal. Chem.* **72**, 5618 (2000).
25. N. H. Finkel, X. Lou, C. Wang, L. He, *Anal. Chem.* **76**, 352A (2004).
26. K. Braeckmans, S. C. D. Smedt, M. Leblans, R. Pauwels, J. Demeester, *Nat. Rev. Drug Discov.* **1**, 447 (2002).
27. D. Dendukuri, D. C. Pregibon, J. Collins, T. A. Hatton, P. S. Doyle, *Nat. Mater.* **5**, 365 (2006).
28. Materials and methods are availabe as supporting material on *Science* Online.
29. R. Hergt *et al.*, *IEEE Trans. Magn.* **34**, 3745 (1998).
30. A. Y. Rubina *et al.*, *Biotechniques* **34**, 1008 (2003).
31. A. V. Vasiliskov *et al.*, *Biotechniques* **27**, 592 (1999).
32. F. N. Rehman *et al.*, *Nucleic Acids Res.* **27**, 649 (1999).
33. D. C. Pregibon, M. Toner, P. S. Doyle, *Langmuir* **22**, 5122 (2006).
34. We gratefully acknowledge support from NSF grant CTS-0304128 and the Dumbros Fellowship.

Inverse Relations Between Amounts of Air Pollution and Orographic Precipitation

Daniel Rosenfeld,[1]* Jin Dai,[2] Xing Yu,[2] Zhanyu Yao,[3] Xiaohong Xu,[2] Xing Yang,[2] Chuanli Du[2]

Particulate air pollution has been suggested as the cause of the recently observed decreasing trends of 10 to 25% in the ratio between hilly and upwind lowland precipitation, downwind of urban and industrial areas. We quantified the dependence of this ratio of the orographic-precipitation enhancement factor on the amounts of aerosols composed mostly of pollution in the free troposphere, based on measurements at Mt. Hua near Xi'an, in central China. The hilly precipitation can be decreased by 30 to 50% during hazy conditions, with visibility of less than 8 kilometers at the mountaintop. This trend shows the role of air pollution in the loss of significant water resources in hilly areas, which is a major problem in China and many other areas of the world.

Large concentrations of submicron particulate air pollution have been documented to suppress precipitation-forming processes by serving as cloud-drop condensation nuclei that form clouds with small drops that are slower to coalesce into raindrops and to glaciate into ice hydrometeors (1–4). This is manifested as less precipitation on the ground when the lifetime of the cloud is shorter than the time for the conversion of cloud water into precipitation. Such short-lived cloud elements typically form as air rises over topographic barriers and evaporate when forced down across the ridge line. Therefore, decreasing trends in the orographic enhancement factor of the precipitation (Ro), which is the ratio between the hill and the upwind plains precipitation, were suggested to reflect the trend of increasing air pollution during that period (5). This hypothesis was supported by the documented reductions of 10 to 25% in the past half century in much of the mountain ranges of the western United States, downwind of major urban and industrial areas (5–8). However, because of a lack of historical records of ambient aerosols, it was not possible to quantitatively relate the amounts of air pollution to Ro. We used a set of measurements taken since 1954 on a mountaintop in central China to quantify the impact of aerosol loading on precipitation in that area.

A meteorological observatory at the top of Mt. Hua (32°23′N, 109°54′E, 2060 m), 120 km east of Xi'an, China (see location in Fig. 1), provides a complete record of four measurements per day of all meteorological elements, except for one measurement per day of precipitation depth. The visibility (VIS) before 1980 was recorded as 10 classes, and the values after 1980 were estimated directly in kilometers, with respect to landmarks of known distance in the mountainous landscape. In order to reduce the effect of relative humidity (RH) on visibility, RH values greater than 40 and less than 99% were converted to the equivalent visibility in dry conditions (i.e., RH <40%). When RH <40%, the visibility did not need to be corrected for RH. The correction formula is expressed as VIS/VIS(dry) = 0.26 + 0.4285 log(100 – RH), where RH is in percent and the log is on the basis of 10. If there was fog or precipitation at all visibility observation times in a day, the visibility of that day was excluded from the corrected visibility series. The daily average values are presented in Fig. 2. The visibility at the mountaintop, shown in Fig. 2, had a marked decreasing trend for the whole measurement period. This trend reflects the trend of increasing air pollution in China (9, 10) during that time. Consistent with the hypothesis that air pollution suppresses orographic precipitation, Ro shows statistically significant decreasing trends of 14 and 17%, with respect to the low-level rain gauges of Huayin and Xi'an (see locations in Fig. 1), respectively (Fig. 3).

The cause for the association of visibility and Ro trends can be tested by ignoring the time factor and testing Ro directly, as a function of the visibility distance. This was done for the uncorrected visibility (Fig. 4), because many of the precipitation events are excluded with the corrected visibility. We hypothesize that reduced visibility indicates the presence of more aerosols and cloud

[1]Institute of Earth Sciences, The Hebrew University of Jerusalem, Jerusalem, Israel. [2]Meteorological Institute of Shaanxi Province, Xi'an 710015, China. [3]Key Laboratory for Cloud Physics and Weather Modification of Chinese Meteorological Association, Chinese Academy of Meteorological Sciences, Beijing 100081, China.

*To whom correspondence should be addressed. E-mail: daniel.rosenfeld@huji.ac.il